ACS APPLIED MATERIALS & INTERFACES

Research Article

www.acsami.org

Co-electroplated Kesterite Bifacial Thin-Film Solar Cells: A Study of Sulfurization Temperature

Jie Ge,*[,†,‡,§] Junhao Chu,*[,†,‡] Yanfa Yan,[§] Jinchun Jiang,[‡] and Pingxiong Yang[†]

[†]Key Laboratory of Polar Materials and Devices (Ministry of Education), School of Information Science Technology, East China Normal University, Shanghai 200241, P. R. China

[‡]Shanghai Center for Photovoltaics (SCPV), Shanghai 200081, P. R. China

[§]Wright Center for Photovoltaics Innovation and Commercialization, Department of Physics and Astronomy, The University of Toledo, Toledo, Ohio 43606, United States

Supporting Information

ABSTRACT: Earth-abundant material, kesterite Cu_2ZnSnS_4 (CZTS), demonstrates the tremendous potential to serve as the absorber layer for the bifacial thin-film solar cell. The exploration of appropriate sulfurization conditions including annealing temperature is significant to gain insight into the growth mechanism based on the substrates using transparent conductive oxides (TCO) and improve device performance. The kesterite solar absorbers were fabricated on ITO substrates by sulfurizing co-electroplated Cu−Zn−Sn−S precursors in argon diluted H_2S atmosphere at different temperatures (475−550 °C) for 30 min. Experimental proof, including cross-section scanning electron microscopy, X-ray photoelectron spectroscopy, X-ray diffraction, UV−vis−NIR transmission spectrum, and Raman and far-infrared spectroscopy, is presented for the crystallization of CZTS on an ITO substrate and the interfacial reaction between the ITO back contact and CZTS absorber. The complete conversion of precursor into CZTS requires at least 500 °C sulfurization temperature. The aggressive interfacial reaction leading to the out-diffusion of In into CZTS to a considerable extent, formation of tin sulfides, and electrically conductive degradation of ITO back contact occurs at the sulfurization temperatures higher than 500 °C. The bifacial devices obtained by 520 °C sulfurization exhibit the best conversion efficiencies and open circuit voltages. However, the presence of non-ohmic back contact (secondary diode), the short minority lifetime, and the high interfacial recombination rates negatively limit the open circuit voltage, fill factor, and efficiency, evidenced by illumination/temperature-dependent $J-V$, frequency-dependent capacitance−voltage ($C-V-f$), time-resolved PL (TRPL), and bias-dependent external quantum efficiency (EQE) measurements.

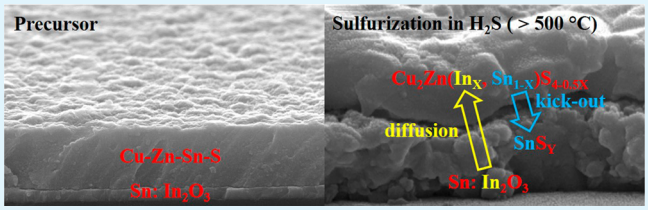

KEYWORDS: *kesterite bifacial solar cell, sulfurization temperature, interfacial reaction, ITO back contact, indium diffusion, tin sulfides*

INTRODUCTION

Thin-film heterojunction photovoltaic (PV) technology demonstrates the tremendous potential to displace electricity generation based on non-renewable fossil fuels because of its reduced material consumption and simple device design. Can thin-film solar devices pervading in the human society be realized only if associated manufacturing costs were made competitive? In this regard, concerns over the application of earth-abundant materials and fabrication methods for preparing high-performance thin-film solar devices arise as the feasible pathways forward in pervasive low-cost PV technology. In thin-film devices, a wide range of earth-abundant materials, such as Zn_3P_2,[1,2] Sb_2S_3,[3−5] SnS,[6−8] PbS,[9] FeS_2,[10] Cu_2S,[11] Cu_2O,[12,13] $CuSbS_2$,[14] Cu_2SnS_3,[15] kesterite Cu_2ZnSnS_4 (CZTS),[16] and hybrid perovskite $CH_3NH_3PbI_3$,[17−19] have been used as the solar absorber, among which CZTS has been getting pronounced attention because of its nontoxic constituents, phase stability, and/or quality for highly efficient solar devices.

Solar Frontier reported an 8.65% efficient solar cell with an ultra-thin 600 nm CZTS absorber made by post-sulfurizing evaporated/sputtered precursors in 2011,[20] and hit a 9.19% record efficiency with a long minority lifetime of 36 ns two years later,[21,22] but no more details on their fabrication processes are disclosed to date. A certified 8.4% efficiency CZTS solar cell with a 600 nm absorber made by post-sulfurization of rapidly co-evaporated metal−sulfur precursor at 570 °C for 5 min was reported by IBM in 2011.[23] In the same year, IBM additionally reported a 7.3% efficiency electroplated CZTS cell.[24] In this work, pre-annealing electroplated metal stacking layers at 350 °C for 30 min was adopted to prepare precursor brass/bronze alloys. The following annealing in sulfur vapor at 585 °C for 12 min finally synthesized desired CZTS absorbers. This fabrication process was then followed by Jiang

Received: February 20, 2015
Accepted: April 14, 2015
Published: April 14, 2015

DOI: 10.1021/acsami.5b01641
ACS Appl. Mater. Interfaces 2015, 7, 10414−10428

et al., leading to an 8.0% efficiency CZTS solar cell in 2013.[25] Meanwhile, Scragg et al. prepared CZTS precursors by reactively co-sputtering $Cu_{65}Sn_{35}$ alloy and Zn targets in pure H_2S atmosphere and yielded a 7.9% efficiency by 570 °C post-sulfurization for 10 min in sulfur vapor.[26] In 2014, Tajima et al. reported an 8.5% certified efficiency using a two-layered CZTS absorber with a Cu content gradient.[27] The first stoichiometric absorber layer was made by sulfurization of sputtered Cu/Sn/ZnS precursor at 580 °C for 20 min in N_2 diluted H_2S (vol. 20%). Then, the other Cu-poor stacking layer of Cu/Sn/ZnS was deposited on the thus-obtained absorber. The final sulfurization preformed at 500 °C for 60 min yielded the CZTS absorber with Cu gradient. This novel structure renders a 0.78 V open circuit voltage that is the best result among the reported kesterite solar cells to date.

These promising results demonstrate the elementary success of fabrication routes based on layer deposition using evaporation, sputtering, and electroplating technology plus post-sulfurization annealing. It should be pointed out that the technology based on electroplating standing out from the other chemical methods exhibits the utmost industrial compatibility for large-scale film deposition by high throughput using low-cost and environmentally benign aqueous solution, whose superiority has been unequivocally verified by the industrial success of electroplated CIGS.[28] As opposed to vacuum-based approaches, electroplating still excels in its lower capital equipment investment and lower energy consumption.[29] Another crucial factor that determines the industrial feasibility of a high efficiency CZTS solar cell depends on viable post-sulfurization annealing strategies. Annealing conditions involving sulfurization temperature, time, and atmosphere (sulfur vapor vs H_2S) causally link and affect the compositional variance, grain size, and crystallization processes leading to CZTS. Two routine annealing strategies, either short annealing (5−20 min) at higher temperatures (570−590 °C) or long annealing (up to 1−2 h) at lower temperatures (500−550 °C), are widely employed to grow CZTS, whereas the former seems more favorable to obtain highly efficient CZTS absorbers in view of the vast majority of the reported works as listed above. Besides, the annealing atmosphere based on either sulfur vapor or H_2S may achieve high performance CZTS absorbers, while the use of H_2S benefits the diffusion of elements and the formation of larger grained CZTS films.[30,31] We have to caution that these tentative conclusions concerning the post-sulfurization annealing are entirely summarized from substrate-type CZTS cells where Mo serves as the back contact.

Additionally, these aforementioned works with respect to highly efficient CZTS solar devices based on ultra-thin 600 nm absorbers manifest kesterite CZTS is an attractive candidate absorber material for bifacial thin-film solar cells which use TCO, i.e. doped ZnO and ITO, layers as the front and back contact. In the bifacial structure, the ultra-thin absorber and transparent electrode layers allow sunlight to pass through the entire device, thus endowing the bifacial device with the potential to serve as solar window/roof. Besides, bifacial devices can harvest sunlight simultaneously from back and front electrodes and thus realize higher output electricity. In order to explore the approaches for the high performance CZTS bifacial device, it is important to learn lessons from the facile CZTS solar devices using Mo back contact and identify areas where the bifacial devices may need unique solutions. In this work, the controllable co-electroplating technology was used to prepare metal sulfide precursors on ITO substrates. Its preliminary success in preparing the precursor layers with smooth and compact morphology and with controllable composition is manifest;[32] thus, the precursor pre-annealing employed in the case of electroplated stack metal layers will be no longer needed, which will additionally simplify and reduce the technique and cost of production. Considering the aspect of post-annealing, in light of the potential thermodynamic instability of TCO itself and in-between TCO and CZTS during high temperature sulfurization (regardless of sulfur vapor or H_2S),[33,34] the exploration of new annealing strategies to know the crystallization of CZTS on ITO substrates is essential for the improvement of bifacial device performance. This requires us to systematically ascertain the unique sulfurization conditions including annealing temperature, time, and atmosphere (sulfur vapor vs H_2S). Herein, we use the annealing method based on low temperatures (475−550 °C) and intermediate annealing time (30 min) to grow CZTS so as to keep ITO back contact as intact as possible. The use of H_2S aims to synthesize larger grained CZTS films at low sulfurization temperatures. The influence of sulfurization temperature on the properties of the absorber layers and the bifacial device characteristics is presented.

EXPERIMENTAL SECTION

Preparation. The cathodic co-electroplated Cu−Zn−Sn−S precursors were prepared on commercial ITO substrates (NSG, 8 Ω/□). A conventional three-electrode assembly with a Ag/AgCl reference, an inert Pt anode, and an ITO conductive glass as the cathode was used. The precursor was deposited at −1.15 V vs Ag/AgCl in potentiostatic mode for 30 min without stirring. The nontoxic aqueous electrolyte (200 mL) consisted of sodium citrate (100 mM) together with potassium tartrate (5 mM) as complexing reagents, metal sulfates of Cu(II) (10 mM), Zn(II) (50 mM), Sn(II) (10 mM) ions, and sodium thiosulfate (5 mM). The post-sulfurization was carried out in a tube furnace ramping at 20 °C min^{-1} and dwelling at 475 °C, 500 °C, 520 °C, 540 °C, and 550 °C for 30 min. The argon diluted H_2S (vol. 5%) atmosphere was supplied continuously into the tube furnace, and a pressure of ∼10 Torr was monitored by a Pirani vacuum gauge. As-sulfurized absorbers were immediately dipped in an alkaline bath for the deposition of an *n-type* CdS layer (approximately 80 nm). The growth of the CdS layer uses chemical solutions of $CdSO_4$ (1.5 mM), thiourea (75 mM), and ammonium hydroxide (1.8 M) at 85 °C. Window layers of i-ZnO/ZnO:Al were sputtered through an aperture mask with an area of 0.07/0.09 cm^2.

Characterization. Scanning electron microscope (SEM) analysis was conducted using Hitachi S4800 FE-SEM. Precursor compositional results were acquired by Oxford X-max energy dispersive X-ray spectroscopy (EDX) equipped with FE-SEM. X-ray diffraction (XRD) data were collected using a Rigaku 69 D/max 2550 V diffractometer with Cu Kα lines (0.15418 nm) in θ−2θ scans operated at 40 kV and 250 mA with a graphite monochromator. Theta calibration was conducted using a standard Si sample prior to the XRD measurement. The transmission of the absorber layer and ITO layer were performed using a Varian Cary 5000 UV−vis−NIR spectrophotometer, where the transmission of the soda lime glass substrate was subtracted in terms of the baseline. Raman spectroscopy (room temperature) was carried out using Nanofinder 30 (TII Tokyo Instruments) with a resolution of less than 1 cm^{-1} under parallel configuration. A polarized 532 nm beam excited by a solid state laser with a laser excitation power of 2 mW was normally incident on the sample surface. Raman shift was calibrated by the single crystal Si at 520.4 cm^{-1}. Fourier Transform Infrared Spectroscopy (FTIR) was carried out using equipment Bruker vertex 80v with a resolution of less than 2 cm^{-1}, with the incident irradiation nearly normal to the sample surface in the reflection mode. X-ray photoelectron (XPS) and X-ray excited Auger electron (XAES) spectra were conducted using an XPS Kratos Axis Ultra DLD spectrometer fitted with the monochromatic Al Kα X-rays.

DOI: 10.1021/acsami.5b01641
ACS Appl. Mater. Interfaces 2015, 7, 10414−10428

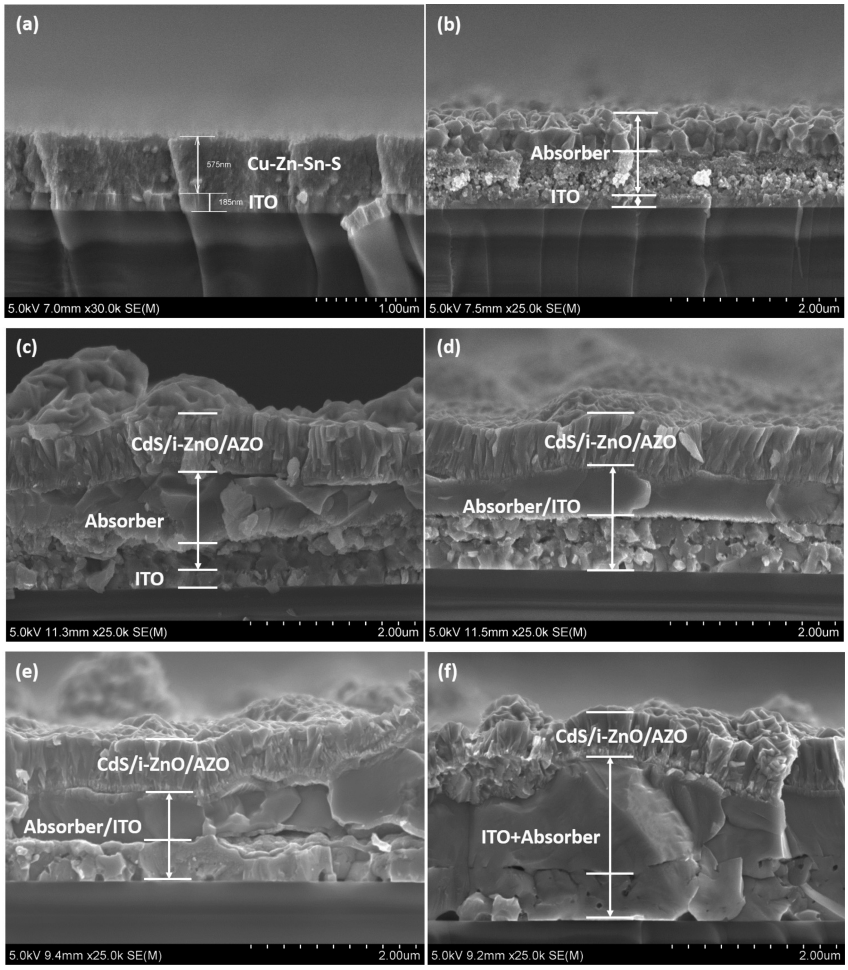

Figure 1. SEM cross-sectional images of the precursor on ITO substrate (a), the sulfurized film at 475 °C (b), and the finished solar cells grown by the sulfurization at the temperatures of 500 °C (c), 520 °C (d), 540 °C (e), and 550 °C (f).

The current−voltage characteristics of the bifacial device for one-side illumination (front and rear) were measured under the AM 1.5 global spectrum with the irradiance set to 1000 W m^{-2} (1 sun; Xe lamp). The bifacial current−voltage characteristics were measured under the simultaneous illumination of a Xe lamp (1 sun) from the front side of a ZnO window layer and a halogen lamp (~1 sun) from the rear side of an ITO back contact. External quantum efficiency (EQE) measurements were performed by a single source illumination system (halogen lamp) combined with a monochromator, with a light beam of 3 × 3 cm^2 illuminating on the samples. A calibrated Si-cell was used as reference for the $J-V$ as well as for the EQE measurements. The frequency dependent capacitance−voltage ($C-V-f$) measurements were performed at room temperature with a DC bias scanning from −0.8 V to +0.8 V using the Dielectric Spectrometer BDS40, and 50 mV rms was used as the testing AC signal with selected frequencies. Time resolved photoluminescence (TRPL) measurements (pulse width: 5 ps) were conducted at 20 K and at room temperature using a closed cycle helium cryostat from Advanced Research Systems and a Hamamatsu R5509-42 NIR PMT detector. The TRPL measurement at room temperature was performed with the help of multiple wavelength channels of the Fianium AOTF due to the low signal. The repetition rate was selected to be 5 and 20 MHz for the measurement at 20 K and room temperature, respectively.

RESULTS AND DISCUSSION

Figure 1 shows the SEM cross-section images of the film before and after sulfurization along with the finished solar cells grown by different temperatures. A compact and uniform layer of metal sulfide precursor was grown on ITO substrate by the co-electroplating technique as shown in Figure 1a. The precursor composition is Sn rich (approximately Cu:Zn = 2:1, Zn:Sn = 0.9:1, S:metals = 0.2:1). The entire films after sulfurization show a bilayered crystalline structure, and the crystalline quality of the films has a close dependence on the sulfurization temperature. The film sulfurized at 475 °C has a particulate-like bottom layer and a better-crystalline upper layer with an average grain size of 300 nm. Increasing the sulfurization temperature gives rise to better crystalline quality and larger grain size (>2 μm) of the absorber. For the samples grown at temperatures ≥520 °C, no clear boundary between ITO and absorber layers is discernible, predicting the occurrence of interfacial reaction between ITO and the absorber layer. With the increased sulfurization temperature, the grains in the bottom absorber layer gradually grow up; ultimately, the bottom absorber layer fully reacts with the ITO back contact and results in complete disappearance of ITO back contact (see Figure 1e and f). The TEM analysis of the bifacial device prepared by 520 °C confirms this interfacial reaction, which results in the In atoms coming from the ITO back contact diffusion into the CZTS absorber layer.[34] The corresponding TEM-EDS suggests that the large grains in the upper layer are heavily tin deficit and slightly sulfur poor (*i.e.* $Cu_{2.040}Zn_{1.000}(Sn_{0.493},In_{0.447})S_{3.677}$). This composition result suggests In will mainly incorporate on the Sn site in the

DOI: 10.1021/acsami.5b01641
ACS Appl. Mater. Interfaces 2015, 7, 10414−10428

CZTS lattice, because of the similarity of the atomic size and the charging state of In (+III) and Sn (+IV). Additionally, the absorber surficial composition results by XPS/XAES indicate valence states of the constituent elements in CZTIS alloy: Cu (+I), Zn(+II), In (+III), Sn (+IV), and S(−II) (Figure S1 in the Supporting Information).

XRD measurements were performed to identify crystalline phases of the films sulfurized at different temperatures and the Cu−Zn−Sn−S precursor (Figure 2). For the precursor (Figure 2a), there is a very wide peak (Δ) located at $2\theta \approx 42-43°$ that corresponds well with brass $CuZn_5$ (PDF 97-005-6276) and bronze Cu_3Sn (PDF 97-005-6282) alloys, and the rest peaks (#) can be entirely assignable to ITO substrate (PDF 97-005-0849). For the film grown at 475 °C, the reflection coming from CZTS becomes considerably visible. However, the observed reflections at 37.603°, 42.008°, and 43.241° arising from $CuZn_5$ and Cu_3Sn alloys (Δ) suggest the complete conversion to CZTS requires higher temperatures than 475 °C. The films grown by the temperatures ≥500 °C present the phase coexistence of tin sulfides and CZTS (PDF 97-018-9286). The film sulfurized at 500 °C shows the trace of SnS_2 phase, proved by the peak at $2\theta = 15.080°$ that agrees well with the 001 peak of SnS_2 (PDF 97-065-0993). As the sulfurization temperature increases, a number of tin sulfide phases starts to form, evidenced by the observation of the intense peaks at 2θ = 26.179°, 27.475°, 31.640°, 31.981°, 39.084°, 44.838°, and 66.563° that respectively correspond to the 201, 210, 301, 400, 131, 141, and 171 peaks of SnS (PDF 97-005-2108). The formation of SnS is due to the decomposition of SnS_2. For the film sulfurized at 550 °C, the diffraction peaks of SnS_2 have disappeared and the number/intensity of diffraction peaks of SnS have remarkably decreased, implying tin sulfides present in the absorber layer were reduced by high temperature because of their high vapor pressures. In order to elucidate the formation of a high density of tin sulfides, comparative XRD results of the sulfurized CZTS films on Mo substrates are presented in Figure S2 in the Supporting Information. Also, tin sulfides are revealed by XRD present in the films on Mo substrates, the formation of which can be attributed to the Sn-rich precursor content. While, as the annealing temperature increases, the reflections of tin sulfides gradually disappear, finally, the film grown at 540 °C on Mo substrate demonstrates a pure kesterite CZTS phase. This observation shows a converse tendency with the films grown on ITO substrates. The appearance of the SnS_2 phase in the film sulfurized at 500 °C on ITO may be assumed as the result of Sn-rich precursor content, since the diffraction intensity of the SnS_2 phase is very close to the counterpart on Mo substrate. However, the apparently increased peak intensity of tin sulfides (SnS and SnS_2), compared to the films grown on Mo substrates, indicates the samples on ITO substrate have more tin sulfide phases produced by higher temperature annealing. We additionally note that the reflections of ITO substrate are no longer observed for the films sulfurized by the temperatures greater than 500 °C. This suggests that high temperature sulfurization using H_2S promotes the reaction of CZTS absorber and ITO back contact, consistent with the SEM observation. Thus, the observation of tin sulfides with abnormally increased amounts in the absorbers should be related to this interfacial reaction.

As additionally shown in Figure 2b where the magnified 112 and 220/204 reflex are given, the reflections of the absorber layers shift toward lower angles (bigger unit cell size) with the increased sulfurization temperatures. Likewise, the calculated lattice parameters increase with the sulfurization temperature as shown in Table 1 accordingly. The films sulfurized at 520, 540, and 550 °C have bigger lattice constants than kesterite CZTS (*s.p.* $I\bar{4}$, a = 5.427 Å, c = 10.868 Å), however still smaller than chalcopyrite $CuInS_2$ (*s.p.* $I\bar{4}2d$, a = 5.523 Å, c = 11.133 Å). Such a large lattice expansion can be explained by the diffusion of In into CZTS, because In has a bigger atomic/ionic radius 1.63/0.8 (+III) Å than Sn 1.41/0.45 (+IV) Å. This is cogent evidence for substitutional diffusion of In into CZTS absorber via ionic exchange with Sn. Higher sulfurization temperatures

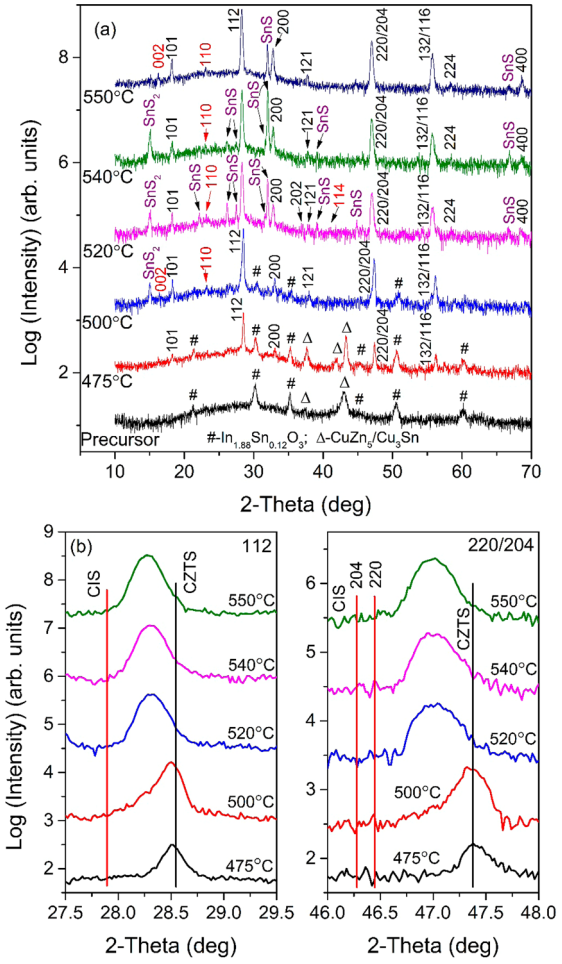

Figure 2. X-ray diffraction patterns of the co-electroplated Cu−Zn−Sn−S precursor on ITO substrate and the absorbers sulfurized at 475−550 °C (a); the magnified reflections of 112 and 220/204 for highlighting (b), with black and red line makers representing the peak positions of KS-CZTS (PDF 97-018-9286) and CH-CIS (PDF 97-006-6865), respectively.

Table 1. Relevant Parameters Derived from XRD Patterns and Raman Spectra of the Absorbers Sulfurized at 500−550 °C

	lattice constants (Å)		dominant A mode	
	a	c	position (cm^{-1})	fwhm (cm^{-1})
500 °C	5.4308	10.8193	328.3 ± 0.0	17.6 ± 0.4
520 °C	5.4615	10.8785	331.4 ± 0.1	13.4 ± 0.4
540 °C	5.4703	10.8859	332.5 ± 0.0	10.5 ± 0.1
550 °C	5.4639	10.9345	332.3 ± 0.0	11.7 ± 0.1

DOI: 10.1021/acsami.5b01641
ACS Appl. Mater. Interfaces 2015, 7, 10414−10428

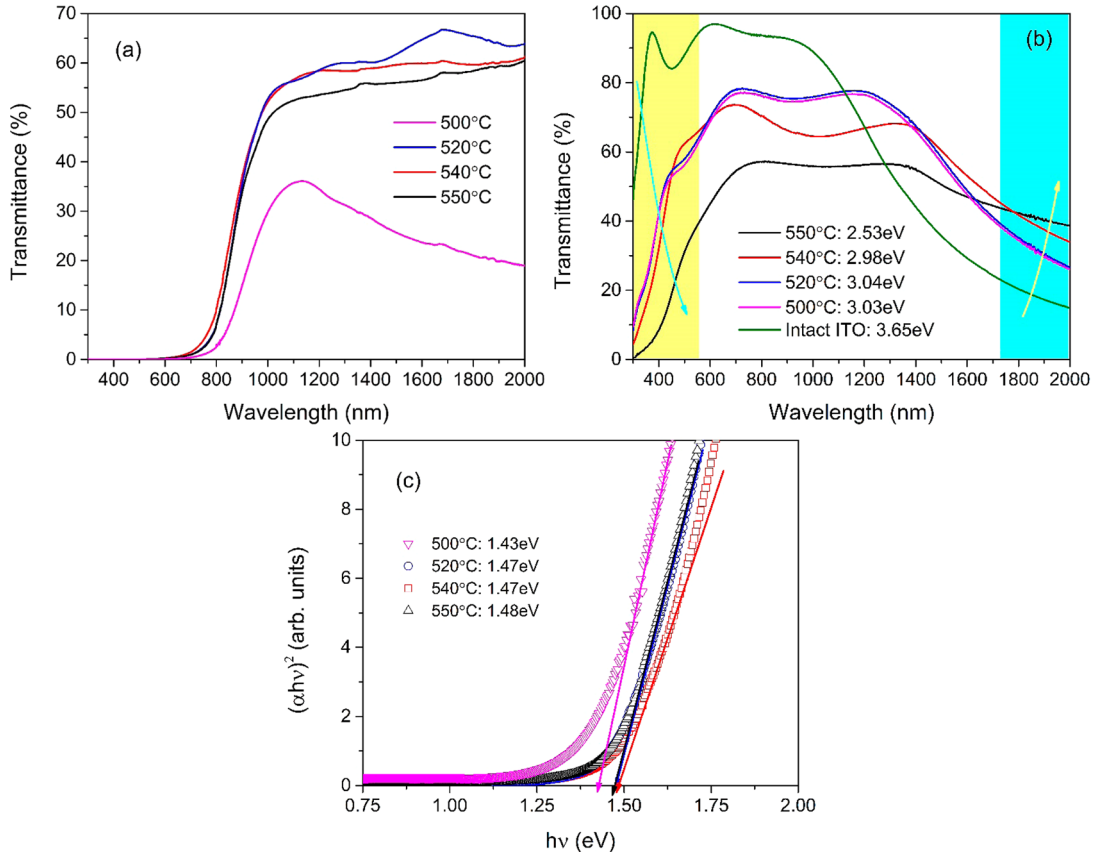

Figure 3. Optical transmission spectra of the absorbers sulfurized at 500−550 °C (a), the transmittance of bared ITO substrates before and after sulfurization at corresponding temperatures (b), and the band gap energy plots for the corresponding absorbers (c). Note that the sulfurization procedure for bare ITO substrates is congruent with that used for the absorbers. The band gap energy (E_g) was estimated using the Tauc plot of $(\alpha h\nu)^2$ vs $h\nu$, where $h\nu$ is the photon energy and α is the absorption coefficient that can be extracted from the transmittance of the absorbers using the relation $\alpha = -d^{-1} \ln T$ (d is the film thickness; T is the film transmittance) on the basis of parabolic approximation.

will cause more In diffusion into absorber layers with more expanded lattices, and more Sn in CZTS will be kicked out by In; thus, more tin sulfides will form and more ITO layer will be consumed. The film sulfurized at 500 °C does not exhibit any lattice expansion as compared with kesterite CZTS, which suggests In might probably just start to diffuse into the film or the content of diffused In in the film is very little at this temperature. Thus, the film grown by 500 °C sulfurization is primarily made of CZTS. As pointed out, we cannot preclude the likelihood of the potential out-diffusion of indium atoms into the films at temperatures $T \leq 500$ °C, while the extent of out-diffusion should be extremely small. Our TEM analysis of the sample grown at 520 °C suggests only 2% of indium out-diffusion into the amorphous Cu_2SnS_3 in the particulate-like underlying absorber layer, which is one intermediate phase leading to CZTS.[34] This predicts the extent of indium out-diffusion into Cu_2SnS_3 should be much lesser at temperatures $T \leq 500$ °C. Besides, it is not very easy for In to diffuse into ZnS, which is another intermediate phase leading to CZTS, due to their larger atomic mismatch. CZTS may likely form, therefore, prior to indium diffusion. As compared to the chalcopyrite/cubic type structures, kesterite produces additional XRD peaks, such as 002, 110, 114, and 006, due to the discrepancy in the metal atomic orderings.[35] The observation of some of these minor reflections (marked in red in Figure 2a) demonstrates the resultant absorber layers still adopt the kesterite structure.

Figure 3 characterizes the optical transmittance (T) of the absorbers sulfurized at 500−550 °C. As shown in Figure 3a, the high transmittance (>50%) in the infrared region typically suggests the absorbers sulfurized by the temperatures greater than 500 °C are characteristic of lower free carrier absorption and thus high resistance. In contrast, the infrared transmittance of the absorber sulfurized by 500 °C still remains as low as the intact ITO substrate (Figure 3c). This demonstrates that the sulfurization temperatures higher than 500 °C can ruin the conductivity of the ITO substrate. Lowering sulfurization temperature may preserve ITO back contact from being degraded; however, low temperature sulfurization (e.g., 500 °C) will result in poorly crystalline absorbers with a high density of band tailing states, evidenced by the observation that the absorption edge of 500 °C−absorber is not as straight as the other absorbers sulfurized using higher temperatures. The transmission spectra of bared ITO substrate before and after sulfurization in diluted H_2S atmosphere are presented in Figure 3b, in order to ascertain how sulfurization temperature influences its optical/electrical properties. In the short wavelength regime, it can be clearly seen that the band gaps of the sulfurized ITO films decrease (i.e., absorption edge shifts to longer wavelength) as the sulfurization temperature increases. The band gap of the ITO film sulfurized at 550 °C, 2.53 eV, is very close to that of In_2S_3.[36] Besides, the color of the ITO films after sulfurization becomes more and more yellow, other than the ITO film annealed at 475 °C that is still

DOI: 10.1021/acsami.5b01641
ACS Appl. Mater. Interfaces 2015, 7, 10414−10428

visually transparent. These observations along with XRD results (Figure S3 in the Supporting Information) indicate the concurrence of In_2S_3 related phases in the sulfurized ITO substrates by the temperatures ≥500 °C, while high temperature sulfurization cannot fully convert ITO into In_2S_3. We also note that the transmittance of these sulfurized ITO films in the infrared region increases with the sulfurization temperature, implying the conductivity of ITO degrades at higher temperatures. Although these sulfurized films remain conductive to some extent as the transmittance still drops down in the infrared region. The remnant ITO layer is not as conductive as the intact one due to the reduced effective thickness and the removal of its dopants. It should be pointed out that sulfurization at temperatures as high as 550 °C using H_2S cannot fully devastate ITO conductivity; that is to say, H_2S cannot convert ITO completely into In_2S_3 at this temperature. Moreover, the absorber film should have protected ITO substrate from being exposed to and damaged by H_2S. However, another striking feature is observed in the transmittance of the infrared region between the sulfurized ITO films (Figure 3b) and the absorbers grown at temperatures greater than 500 °C (Figure 3a). At these temperatures, the sulfurized absorbers on ITO substrates should have had lower transmittances than the corresponding sulfurized ITO films since the ITO substrates were covered by such thicker absorber layers that H_2S was very difficult to penetrate thorough and damage the underlying ITO films; unexpectedly, this was not the case. This indicates that the contact to CZTS absorber at temperatures higher than 500 °C can cause remarkable conductivity loss of the ITO substrate, irrelevant to the use of H_2S.

Based on the experimental results above, one possible route for the interfacial reactions at ITO back contact can be expressed as

$$3H_2S + In_2O_3 \xrightarrow{T\geq 500^\circ C} In_2S_3 + 3H_2O \quad (1)$$

and

$$x In_2S_3 + 2Cu_2ZnSnS_4 \xrightarrow{T>500^\circ C} 2Cu_2Zn(Sn_{1-x}, In_x)S_{4-0.5x} + 2xSnS_2 \quad (2)$$

First, ITO substrate reacts with H_2S to form In_2S_3 at temperatures $T \geq 500$ °C; then In_2S_3 reacts with CZTS to form CZTIS and tin sulfides at the temperatures $T > 500$ °C. As demonstrated previously, the reaction of ITO with H_2S significantly began at 500 °C. However, no In_2S_3 intermediate phases, to a considerable extent, were discovered by XRD along with the following FTIR spectra in these sulfurized CZTS films (Figure 2a), especially for the film sulfurized by 500 °C. One possible interpretation is that the absorber on the top protected ITO from being damaged by H_2S; thus, the reflections of ITO remained resoluble by XRD for the 500 °C sulfurized film. Meantime, it cannot explain the disappearance of ITO substrates from XRD patterns at higher annealing temperatures in Figure 2a. Thus, we assume the likelihood of the occurrence of this interfacial reaction route is very little. However, we cannot rule out the potential presence of this reaction, because the amount of intermediate phase In_2S_3 is possibly too small to be resolved by XRD or FTIR.

Experimentally, a new interfacial reaction at ITO back contact in bifacial kesterite solar cells chalgenized using hydrogen-free atomphere has just been revealed and can be expressed as[37]

$$2x In_2O_3 + 4Cu_2ZnSnS_4 \xrightarrow{T>500^\circ C} 4Cu_2Zn(Sn_{1-x}, In_x)S_{4-0.5x} + 3xSnO_2 + xSnS_2 \quad (3)$$

This interfacial reaction indicates high temperature sulfurization using sulfur vapor can stimulate the substitutional diffusion of In into CZTS via Sn sites to a considerable extent due to their similar atomic/ionic radii and additionally contributes the formation of SnO_2 interfacial layer underneath the absorber large-grain layer.

We assume this reaction is also valid during the sulfurization using H_2S in this work, while no SnO_2 phase was observed, which can be understood by the strong reducibility of H_2S, namely,

$$2H_2S + SnO_2 \xrightarrow{T>500^\circ C} SnS_2 + 2H_2O \quad (4)$$

Herein, we preferentially assume the second reaction route may interpret the interfacial reaction more reasonably. As the annealing temperatures rise, more Sn from CZTS will be kicked out to form SnO_2; thus, more and more SnS_2 will be formed via eq 4. Actually, these two reaction routes above can be both merged and formulated into one reaction, namely,

$$3xH_2S + x In_2O_3 + 2CuZnSnS_4 \xrightarrow{T>500^\circ C} 2Cu_2Zn(Sn_{1-x}, In_x)S_{4-0.5x} + 2xSnS_2 + 3xH_2O \quad (5)$$

which corroborates this interfacial reation appropriately. It may additionally lead to the formation of a SnS_2 layer distributing underneath the large-grain layer of the absorber. We indeed observe a thin layer in-between the upper and bottom absorber layers as shown in Figure 1e. This thin layer may possibly correspond to layer-structured SnS_2,[38] SnS, and/or the mixture of them.

Figure 3c gives the band gap estimation results of these absorbers, where the absorber sulfurized at 500 °C presents the lowest band gap value of 1.43 eV, due to the severe band tailing. The other absorbers show the congruent band gap values of 1.47−1.48 eV with kesterite CZTS, albeit with In diffusion into CZTS. For the kesterite CZTS, the conduction band minimum (CBM) is composed by the antibonding state of the Sn-5s/S-3p orbitals.[39] In has a higher 5s orbital than Sn; therefore, it will upshift the conduction band and consequently increase the band gap if In incorporates on the Sn site. On the other hand, In incorporation will result in the lattice expansion and increase Sn−S bonding length. It will ultimately reduce the hybridization of Sn and S, downshift the CBM, and thus decrease the band gap. These two opposite factors will compensate each other, and the CBM will not shift very much. Additionally, the valence band maximum (VBM) primarily consists of Cu-3d/S-3p orbitals; therefore, substitution of Sn with In will not affect the VBM remarkably. Overall, the partial substitution of Sn with In has little impact on the fundamental band gap structure of kesterite CZTS. (Herein, we rectify the explanation regarding the band gap evolution in our previous work.[34]) Likewise, the effective mass (m^*) of CZTIS alloy should not be altered significantly by In incorporation, because it is closely correlated with band gap (*i.e.* $m^* = \hbar^2/[\partial^2\varepsilon(k)/\partial k^2]$, with $\varepsilon(k)$ being the eigenvalue of the band edge and k being the

DOI: 10.1021/acsami.5b01641
ACS Appl. Mater. Interfaces 2015, 7, 10414−10428

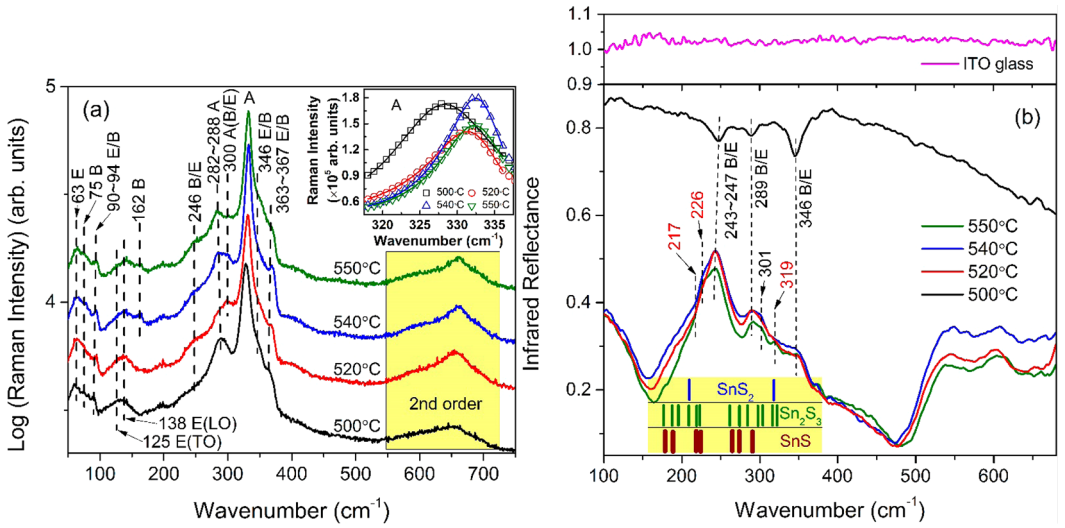

Figure 4. Polarized Raman (a) and far-IR (b) spectra of the absorbers sulfurized at 500−550 °C. (a) inset: the enlarged dominant A modes, with the peaks being fitted using the Lorentzian curve. (b) top-panel: the IR reflection of ITO substrate. (b) inset: colorful line markers showing the IR active modes of tin sulfides.[40−42]

wavevector), but it might be increased by the elastic scattering with phonons, actual structural defects, and/or impurities. Besides, the absorption coefficient will not be altered much since the contribution of the In-5s orbital to the valence band edge is not so apparent that no significant change is observed experimentally.

The absorbers sulfurized at 500−550 °C are further examined using polarized Raman and far-IR spectroscopy (Figure 4). The Raman spectra (Figure 4a) show the visibly intense peaks, which correspond well to the vibrational character of kesterite CZTS. No SnS_2 (205 and 315 cm^{-1}) or SnS (95, 165, 192, and 220 cm^{-1})[43] phases were identified by Raman spectroscopy, owing to the limited penetration depth of the Raman laser. This suggests these tin sulfides segregate underneath the upper large-grain absorber layer.[44] Notably, the appearance of the intense peak at 300 cm^{-1} with the increase of annealing temperature might probably be related to the potential disordering of atomic arrangement in the lattice triggered by the incorporation of In.[45,46] In addition, the discrepancy still exists in the symmetry identification of this peak: it might be assignable to either A mode or B/E mode in some experimental works.[46,47] The analysis of Raman bands provides a sensitive indicator to the film crystallinity.[48] The magnified dominant A modes (328.3−333.5 cm^{-1}) were fitted by Lorentzian curves as shown in the Figure 4a inset, and the fitted peak position and full-width at half-maximum (fwhm) are shown in Table 1. It can be seen that the A mode shifts slightly to higher frequencies and its fwhm decreases as the sulfurization temperature increases. The film sulfurized at 500 °C has the smallest and the most broadened bandwidth of the A mode, suggesting its lowest crystalline quality owing to its low annealing temperature. Annealing at higher temperatures results in the enhancement of crystallinity and thus reduced bandwidth (i.e., increased phonon lifetime and smaller correlation length) as well as the blueshift of the dominant A mode. Considering the other aspect, the increased sulfurization temperature leads to more In diffusion into CZTS forming a higher density of lattice defects (mainly In_{Sn} and V_S). The presence of such defects in a great amount will promote additional phonon scattering in the CZTIS alloy to the Raman line and consequently result in the increased bandwidth of the dominant A modes. Thus, these two factors, In incorporation and the elevation of sulfurization temperature, will compete to determine the bandwidth of Raman spectra. As seen, the bandwidth of the film sulfurized at 550 °C is bigger than the one grown by 540 °C because of more In doping into CZTS. Considering the aspect of the peak position of the A mode, it will shift to lower frequencies (red shift) due to the reduced force constant by the increased lattice constant, wherefore, CZTIS alloy has a smaller A mode than pure CZTS (336−339 cm^{-1}). However, the red shift of the film sulfurized at 500 °C with the A mode located at around 328 cm^{-1} should possibly arise from the disorder effect in the cation sublattice due to the lower annealing temperature, rather than In incorporation.

Complementary to the Raman spectroscopy, the far-IR spectra in Figure 4b additionally identify SnS_2 and SnS present in the resultant films, evidenced by the appearance of peaks at 217, 226, and 319 cm^{-1}. Another intense peak at 301 cm^{-1} observed in far-IR spectra may be assignable to one of the vibrational bands of Sn_2S_3; however, no Sn_2S_3 was resolved by XRD. Thus, this peak may very likely arise from one of the B/E modes of kesterite CZTS, given the selective rule where only the B/E modes can be observed by IR spectra. The other peaks/valleys can be entirely assignable to CZTS, wherein the peak centered at 282−289 cm^{-1} resolved simultaneously by far-IR and Raman spectra demonstrates the presence of very close phone frequencies produced by A and B/E symmetry. Notably, the far-IR spectra of these absorbers sulfurized at 500−550 °C show quite distinct vibrational absorption features. At sulfurization temperature of 500 °C, the film shows a vibrational valley in the far-IR spectrum, in striking contrast to the vibrational peaks of the other films. This directly relates with the variance of the conductivity of ITO back contact.[32] The observed vibrational absorption valleys for the film sulfurized at 500 °C suggest its ITO back contact is still as conductive as the intact one. The conversion of the vibrational valleys into peaks for the films sulfurized at 520, 540, and 550 °C, however, suggests the degradation of ITO back contact after sulfurization, consistent with the observation of transmission spectra (Figure 3a).

DOI: 10.1021/acsami.5b01641
ACS Appl. Mater. Interfaces 2015, 7, 10414−10428

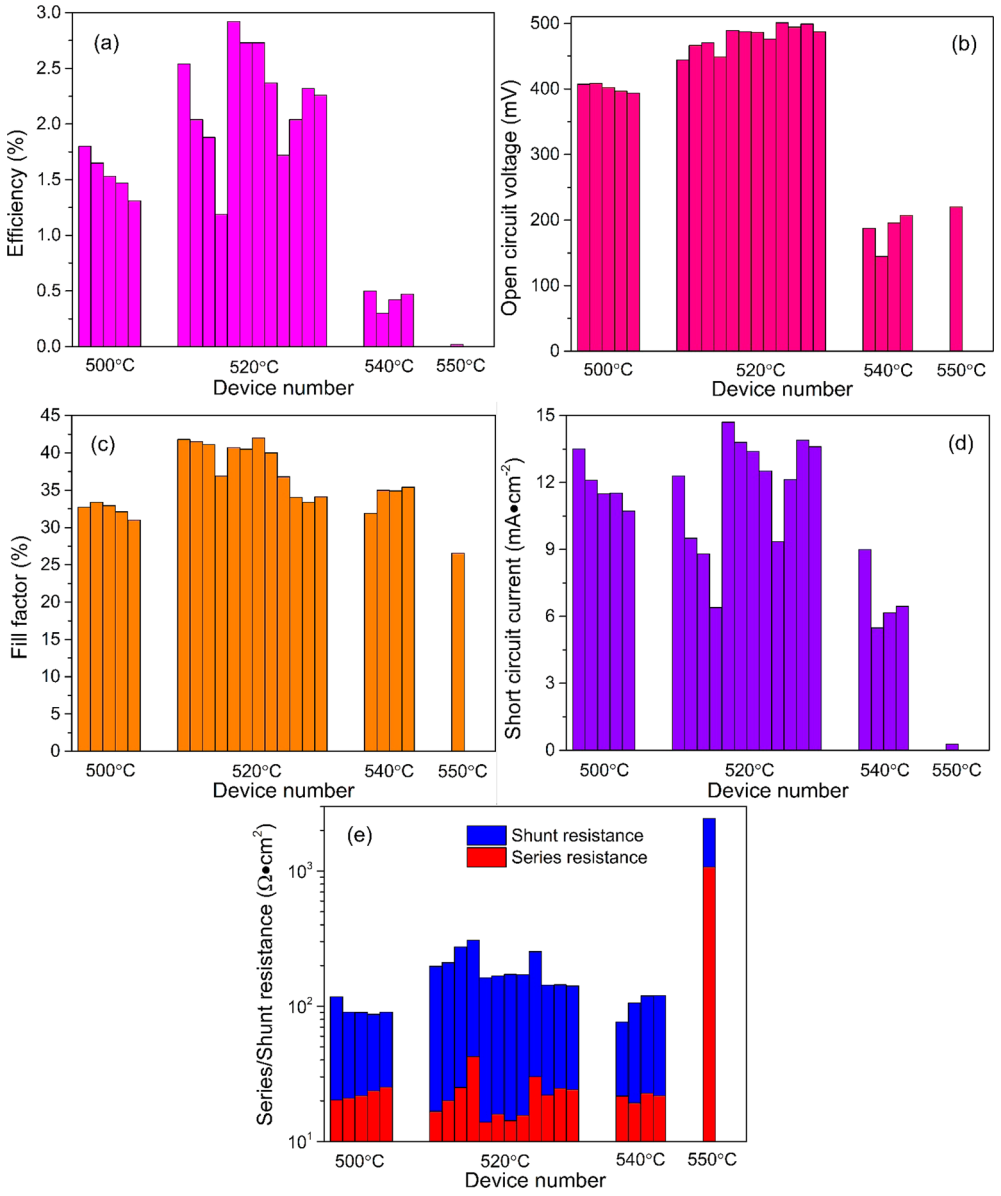

Figure 5. Comparison of the device characteristics [(a) efficiencies, (b) open circuit voltages, (c) fill factors, (d) short circuit current densities, and (e) series/shunt resistances] under front illumination obtained from different sulfurization temperatures: 500−550 °C.

Figure 5 summarizes the characteristics of the corresponding devices obtained from different temperatures under front illumination. The devices obtained from 520 °C sulfurization present the best efficiencies ($eff \approx 1.2-2.9\%$) and open circuit voltages ($V_{OC} \approx 0.45-0.5$ V). Lower sulfurization temperature (500 °C) yields the lower V_{OC} (≈ 0.4 V), which is possibly due to lower material quality and severe band tailing proved by transmission. Although obtaining solar cells with normal $J-V$ curves at higher temperature sulfurization (540 and 550 °C) is very hard, some mini-cells still have somewhat V_{OC} and J_{SC} as shown in Figure 6. Such bad device performances should be contributable to the severely degraded ITO back contact. Overall, these devices based on ITO back contact are still limited by the low fill factors (FF). The best values of FF are obtained to be 42% for the cells sulfurized by 520 °C. The low FF issue should pertain to the low shunt resistance (R_{Sh}), low V_{OC}, and big series resistance (R_S).

Figure 6a−d and Table 2 give $J-V$ curves and corresponding electrical parameters of the four representive mini-cells sulfurized at 500 and 520 °C, under rear/front/bifacial illumination. Compared to front illumination, bifacial illumination increased short circuit currents (J_{SC}) and efficiencies but decreased the cell V_{OC}. In theory, the maximum cell V_{OC} is determined by the splitting of quasi-Fermi levels in the $p-n$ junction. Thus, bifacial illumination should have enabled higher V_{OC}, because more induced photo-generated carriers can move the Fermi levels to the band edges and increase their splitting; however, this is not the case. This reduced V_{OC} under bifacial illumination can be explained by the presence of a non-ohmic back contact or a secondary junction, which may produce a bigger PV voltage as opposed to the front $p-n$ junction under bifacial illumination.[34,49] These cells additionally show parasitic effects including the light-dependent R_{Sh} and R_S, probably originating from the secondary junction or the non-ohmic back contact, and the improved photoconductivity of the CdS layer, respectively. The best V_{OC} among these finished bifacial cells is just greater than 0.5 V (Cell-4) as shown in Table 2, still lower than that of our CZTS cells on Mo substrate (>0.6 V). The

DOI: 10.1021/acsami.5b01641
ACS Appl. Mater. Interfaces 2015, 7, 10414−10428

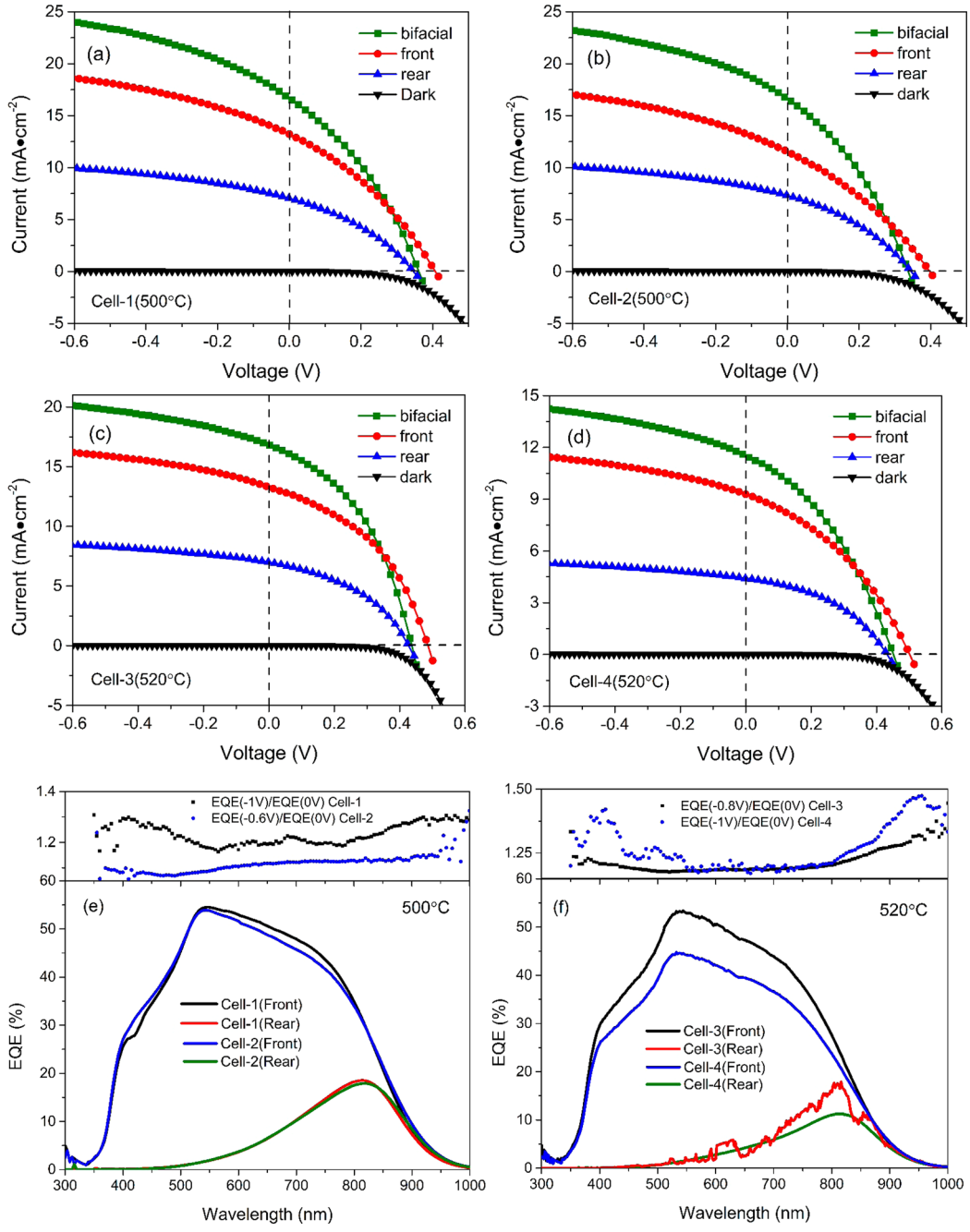

Figure 6. *J*–*V* curves of the typical bifacial cells obtained from 500 °C [(a), (b)] and 520 °C [(c), (d)] under front, rear, and bifacial illumination and in the dark; the EQE curves under front and rear illumination of the bifacial cells obtained from 500 °C (e) and 520 °C (f), with the ratios of EQE curves under negative bias and zero bias for the front illuminations being given in the top panels accordingly.

indium incorporation into CZTS might increase the cell V_{OC} due to the increased carrier density and mobility.[50] The presence of the non-ohmic back contact or the secondary diode may be partially responsible for this low V_{OC} issue because the large Schottky-like barrier height can reduce the effective built-in potential (V_{bi}) of the front junction and thus the cell V_{OC}.[51,52]

The EQE curves under front and rear illumination of the corresponding devices are given in Figure 6e and f. The front EQE curve gradually decaying in the long wavelength regime suggests a lower collection efficiency in the bulk of the absorber. Similar issues have been found in other higher performing CZTS devices. This implies the recombination rate is high at the back contact region where the crystalline defects, such as the segregation of secondary phases and/or Kirkendall voids,[24,27] prevail. Besides, the loss at longer wavelength may be additionally caused by short carrier diffusion length and/or the limited depletion width toward the absorber. To ascertain the carrier collection loss mechanism, the front illuminated EQE measurement under reverse biases was conducted, and the ratios of EQE(reverse bias)/EQE(zero bias) are plotted on the top panel of Figure 6e and f. As expected, the increased EQE ratios at longer wavelength confirm the minority carrier losses in the quasi-neutral region. However, this may also be due to the severe rear side recombination. Another facet of the biased EQE issue that the EQE ratios (other than Cell-2) increase at

DOI: 10.1021/acsami.5b01641
ACS Appl. Mater. Interfaces 2015, 7, 10414–10428

Table 2. Device Parameters for the Typical Bifacial Cells Obtained from 500 and 520 °C under Front, Rear, and Bifacial Illumination and in the Dark[a,b]

	illumination	*eff* (%)	V_{OC} (mV)	J_{SC} (mA cm^{-2})	*FF* (%)	R_S (Ω)	R_{Sh} (Ω)	V_{OC} deficit (V)[c]
Cell-1 (500 °C)	rear	0.9	346.2	7.0	35.0	309.9	1282.1	
	front	1.8	407.3	13.5	32.7	224.2	1079.6	1.04
	bifacial	2.1	361.2	16.7	34.1	144.6	517.0	
Cell-2 (500 °C)	rear	0.9	344.9	7.3	35.0	304.9	1256.6	
	front	1.5	396.7	11.5	32.1	263.3	704.8	1.04
	bifacial	1.9	337.1	16.6	34.3	137.8	519.5	
Cell-3 (520 °C)	rear	1.2	426.9	7.0	41.2	335.7	4528.1	
	front	2.7	486.2	13.4	42.0	203.7	2252.2	1.00
	bifacial	3.1	436.7	16.9	42.0	152.9	1931.7	
Cell-4 (520 °C)	rear	0.8	432.0	4.4	41.9	591.2	7667.2	
	front	1.7	500.8	9.4	36.8	429.9	3194.0	0.97
	bifacial	1.9	451.5	11.6	36.6	333.0	2533.6	

[a]Cell area: Cell-1 and Cell-2 are 0.09 cm^2; Cell-3 and Cell-4 are 0.07 cm^2. [b]The efficiencies were entirely calculated from 1−sun light intensity. Note: the effective light intensity incident on the front *p*−*n* junction varies with illumination modes in the order of bifacial > front > rear, owing to the absorption loss arising from the bottom absorber layer at the back junction and ITO substrate. [c]V_{OC} deficit is defined by $E_g/q - V_{OC}$, where q is the elementary charge, V_{OC} indicates the ones under front illumination, and the band gap values (E_g) are estimated from the EQE curves under front illumination via the plots of $[h\upsilon \times \mathrm{In}(1 - EQE)]^2$ *vs* $h\upsilon$: Cell-1 (1.45 eV); Cell-2 (1.44 eV); Cell-3 (1.48 eV); Cell-4 (1.47 eV).

shorter wavelength suggests a lower collection efficiency close to the absorber/emitter interface where the holes recombine at higher rates as the minorities if the depletion region was extended a little bit further into the absorber due to lower carrier concentration. We additionally note that the EQE ratios are well above 1.05 over the entire wavelength, which suggests severe recombination present at the interface or near the junction as revealed by the biased EQE.[53] Another hand, the rear illuminated EQE curves show a very weak response regardless where the carriers are generated, particularly in the short wavelength region (300−500 nm). This should be due to the presence of the strong absorption and recombination loss at the rear interfacial layer attributed to inadequate photogenerated carriers reaching the space charge region and short minority carrier diffusion length.

The time-resolved photoluminescence (TRPL) technique was additionally used to evaluate the minority lifetime of Cell-4, which has the best V_{OC} (Figure 7). The two-exponential model

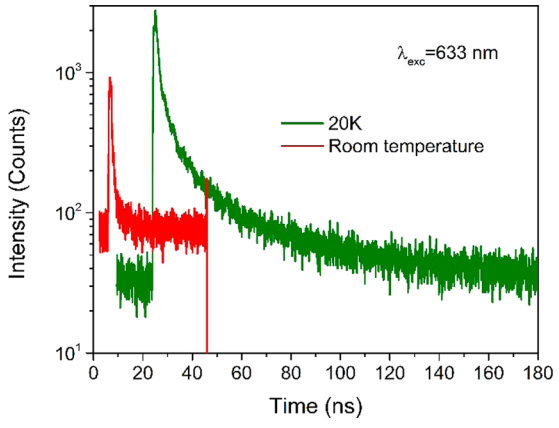

Figure 7. TRPL decays of Cell-4 measured using an excitation wavelength of 633 nm at 20 K and room temperature, with the detection wavelength of 1060 nm for 20 K and 1040 nm for room temperature.

(with deconvolution of the system response function) was applied in data fit of TRPL curves: $I_{PL} = A_1 \exp(-t/\tau_1) + A_2 \exp(-t/\tau_2)$, where I_{PL} is PL intensity, t is time, and A_1/A_2 are amplitudes of τ_1/τ_2 decay components. For 20 K, we yield A_1 = 4080.14, τ_1 = 11.44 ns, A_2 = 104.22, and τ_2 = 161.11 ns. At room temperature, we yield A_1 = 0.085, τ_1 = 112 ps, A_2 = 0.0036, and τ_2 = 1.56 ns. The mean decay time can be determined as $\langle\tau\rangle = (\tau_2A_2 + \tau_1A_1)/(A_2 + A_1) \approx 15.16$ ns (20 K) and 0.17 ns (room temperature). This remarkable increase in the average decay time (i.e., $\langle\tau\rangle$) at low temperature by 2 orders of magnitude can be understood by the presence of electrostatic potential fluctuation that originates from charged defects and forms band tailing.[54] Thus, the presence of severe band tailing negatively limits the minority lifetime at room temperature. Low lifetime will negatively limit the V_{OC} and QE response (*i.e.* J_{SC}) by increasing reverse saturation current and reducing minority diffusion length, respectively. Although In incorporation causes a high density of defect complexes, such as $[2\mathrm{In}_{\mathrm{Sn}}^{-} + \mathrm{V}_{\mathrm{S}}^{2+}]$, the dielectric constant of the alloy additionally plays an important role in determining the fluctuation amplitude. High dielectric constant may favor mitigating this fluctuation. Experimentally, the dielectric constants for $CuInS_2$ and CZTS are 10 and 6.7, respectively.[55,56] The In substituted CZTS kesterite material may have the intermediate dielectric constant due to the features of the alloy. In other words, In incorporation may enhance the dielectric constant of CZTS more or less, which may in turn alleviate the negative impact of the band tailing coming from the charged defects. Otherwise, we are still short of adequate understanding of the exact defect distribution in bulk/surface of this new alloy CZTIS that also determines the minority lifetime of materials: *which defects are electrically benign or detrimental, and which kind of composition can form begin defects and extract maximum photovoltaic efficiency?*

In order to evaluate the back barrier height, we measured the dark current−voltage characteristics at the temperature range of 290−220 K (J−V−T) of Cell-4 with the best V_{OC} (Figure 8a). In our previous work,[34] two equivalent methods were used to

DOI: 10.1021/acsami.5b01641
ACS Appl. Mater. Interfaces 2015, 7, 10414−10428

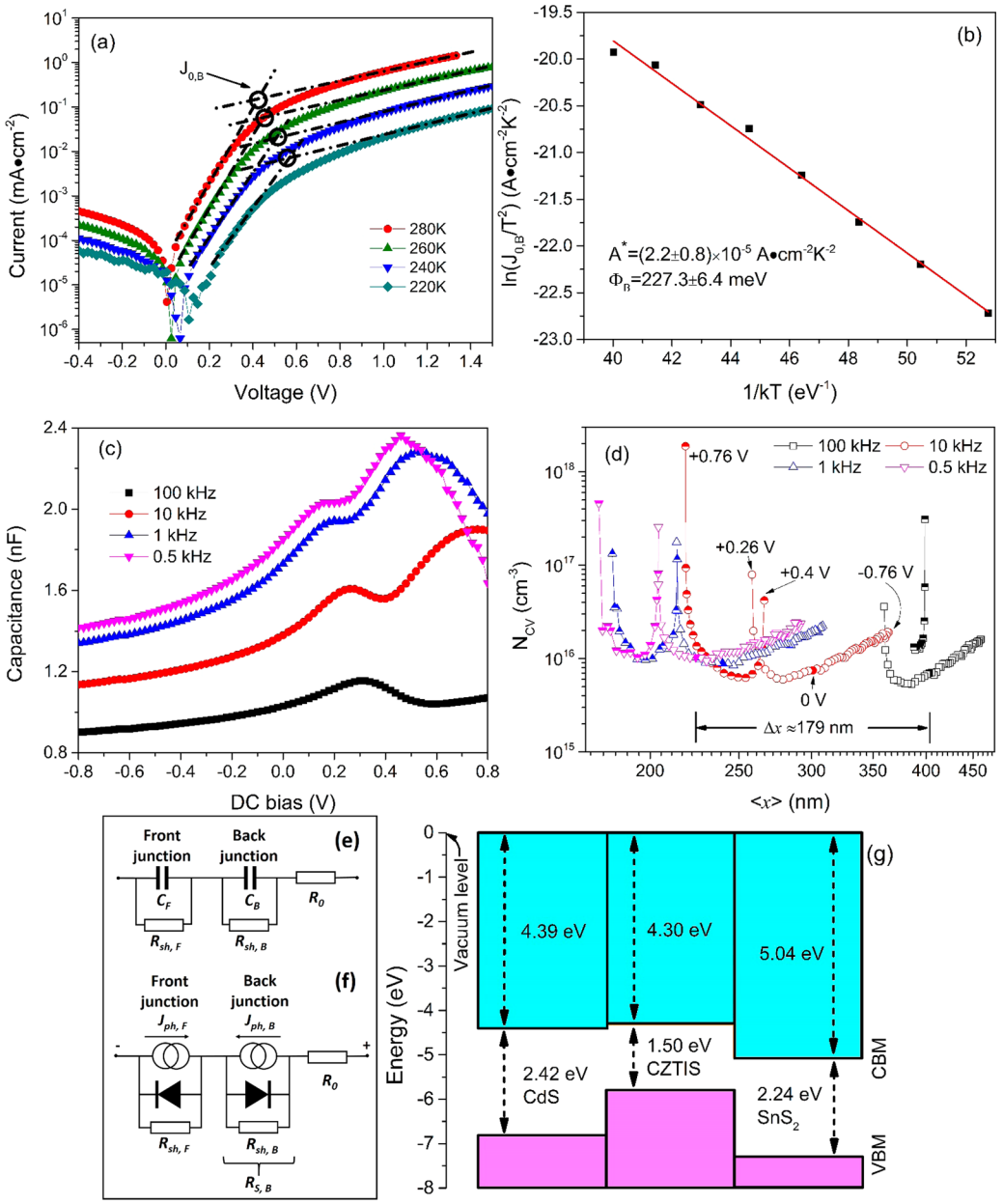

Figure 8. Electrical characterization of Cell-4: (a) semi-logarithmic representation of $J-V$ characteristics under variation of the temperature from 220 to 290 K; (b) the Arrhenius plot of $J_{0,B}(T)$ yielding the barrier height (Φ_B) and effective Richardson constant (A^*) of the back junction; (c) the frequency dependent capacitance–voltage scans ($C-V-f$); (d) the logarithmic representation of $C-V$ derived net charge carrier profiles (N_{CV} vs $\langle x\rangle$) (solid symbols correspond to the N_{CV} calculated at 0 V; open symbols represent the net charge carrier of the front junction; half-open symbols represent the back junction; $\langle x\rangle$ is the distance from the junction; the dielectric constant ε_r takes 6.7, the same value with CZTS); (e and f) device equivalent AC and DC circuit models, respectively, where $R_{sh,F}$ and $R_{sh,B}$ are shunt resistances of front and back junction in light/dark, respectively; (g) band offset diagram of *n-type* CdS/*p-type* CZTIS/*n-type* SnS_2 using a vacuum alignment procedure and that of CZTS for reference based on the calculated result.[38,62]

analyze the dark $J-V-T$ data, and consistent results of barrier height were achieved. Herein, the method developed by Sites and his co-workers is implemented to access the back barrier.[57] This method gives a good approximation of the saturation current density of the back junction $J_{0,B}(T)$ at specific temperatures that can be derived from the intercept point of the pre-rollover and post-rollover slopes as shown in Figure 8a. Moreover, $J_{0,B}(T)$ can be expressed as, $J_{0,B}(T) = A^*T^2 \exp[-\Phi_B/(n_B kT)]$, where k is the Boltzmann constant, Φ_B is the barrier height at back contact, A^* is the effective Richardson constant, and n_B is the ideality factor of the back junction. This expression provides a direct path to the barrier height via the nonlinear fitting; however, the multivariable coefficients of temperature, Φ_B and n_B, within the exponential term make it impossible. In order to access Φ_B, n_B is supposed to be unity under the assumption that the passage of the current over the back contact is mostly dominated by thermionic emission. Thus, the transformation of the above $J_{0,B}(T)$ expression, i.e. Arrhenius plot of $\ln(J_{0,B}T^2)$ vs $1/kT$, makes it possible to yield $\Phi_B = 227.3 \pm 6.4$ meV and $A^* = (2.2 \pm 0.8) \times 10^{-5}$ A cm^{-2} K^{-2} as shown in Figure 8b. This barrier may reduce the effective V_{bi} by 227 mV and thus limit the cell V_{OC}. The series

DOI: 10.1021/acsami.5b01641
ACS Appl. Mater. Interfaces 2015, 7, 10414–10428

resistance due to the back barrier at room temperature can be estimated to be $R_{S,B}(T) = k/(qA^*T)\exp[-\Phi_B/(kT)] \approx 82\ \Omega\ cm^2$. On the other hand, the cell series resistance in dark at room temperature can be fitted to be 161 Ω cm^2 using Sites's method. The difference of these two series resistances, 79 Ω cm^2, primarily originates from the increased resistance of ITO back contact (R_0). Thus, it can be concluded that both the degraded ITO back contact along with the high back barrier account for the large series resistance of the device.

This cell was additionally characterized by the frequency dependent capacitance−voltage technique ($C-V-f$) at room temperature. As shown in Figure 8c, the $C-V$ curves under varied frequencies entirely feature two maxima at forward bias ranges. They predict the presence of the back junction (either Schottky-like back contact or secondary diode) that starts to limit the current, shares the DC/AC voltage with the front junction, and ultimately contributes to the second maxima at higher forward bias. A similar anomaly in $C-V$ curves has been reported in CdTe, CIGS, and CIS solar devices.[58−60] For the 10 kHz profile, at low voltages ≤0.26 V, the measured capacitance corresponds to that of the front junction C_F, because the front junction (i.e., cell junction) primarily limits the current and shares the entire applied voltage; at high voltages ≥0.4 V, the capacitance of the back junction starts to limit the current, and most applied voltages will drop over the back junction; thus, its capacitance C_B is measured. At intermediate voltages, the measured capacitance corresponds to the series connection of C_F and C_B (*i.e.* $C_FC_B/(C_F + C_B)$), which leads to a minimum between the two maxima in $C-V$ curves. As discussed before,[34] the measured device capacitance may additionally show a strong dependency of the measuring frequency in the case of the presence of back contact, which causes the profiling distance shift (Δx) for the different measuring frequencies. The big shift $\Delta x \approx 179$ nm between 100 kHz and 0.5 kHz profiles (Figure 8d) actually relates to the variance in depletion width of the back junction, which in turn depends on the barrier height and the impurity density near the back junction. The $C-V$ derived net charge carrier profiles (Figure 8d) accordingly demonstrate two branches which respectively correspond to the net charge carrier levels in the vicinity of the front (e.g., the bias range of −0.76 V to 0 V to +0.26 V for the 10 kHz profile) and back (e.g., the bias range of +0.26 V to +0.76 V for the 10 kHz profile) junctions. We can simply read the net charge carrier densities near front and back contact from the bottom of the corresponding branch of N_{CV} profiles. The net charge carrier density near the front and back junction are nearly at the same level (e.g., 6.0×10^{15} cm^{-3} near front junction and 6.2×10^{15} cm^{-3} near back junction for 10 kHz profile), other than the profile measured at 100 kHz, where the profile is confined by the limited forward bias, while the doping levels in the vicinity of the back junction should have been much higher than that of the front junction due to the problematic bottom absorber layer where numerous crystalline defects prevail. Besides, these crystalline defects in the bottom absorber layer actually provide the effective tunneling paths such that the current transports through the back contact via hopping between sub-band gap states, which should have benefited from ohmic contact.[13,34] In addition, we do not observe any severe current blocking behavior (Schottky-like back contact or secondary back junction) present in the bifacial devices fabricated using sulfur and selenium vapor.[37] These observations therefore require us to re-evaluate the origin of the back junction for these bifacial devices in this work. The specialty of these bifacial devices fabricated using H_2S gas resides in the interfacial layer of tin sulfides underneath the upper absorber layer. SnS_2 and/or Sn_2S_3 may be *n-type* semiconductors due to V_S, as proved by experiment and theory.[38,61] Hence, this interfacial layer of tin sulfides may likely form another $p-n$ junction with the upper absorber layer opposing to the front junction, and the VB offset as high as 1.50 eV will form a large barrier that suppresses the hole transport across the ITO to the absorber layer (Figure 8g). This proposed hypothesis may also elucidate well the same doping level near the front and back junctions, as they both corresponds to the same upper absorber layer. Chemical etching using ammonium sulfide solution can selectively remove tin sulfides phases,[63] whereas it may not succeed for our samples because tin sulfides phases are buried at the back contact region rather than the film top. On the other hand, the segregation of SnS_2 at the rear side of absorbers may positively prevent the device from the shunting issue due to its high resistance feature.[44,64]

CONCLUSION

In this work, the post-annealing approach based on a low-temperature range from 475 to 550 °C and an intermediate duration 30 min along with the use of argon diluted H_2S was selected to sulfurize co-electroplated Cu−Zn−Sn−S precursors on ITO substrate, in order to explore the appropriate annealing temperatures for the crystallization of CZTS on ITO substrate, which demonstrates a great significance to the optimization of kesterite bifacial devices. The complete conversion of precursor into CZTS will be finished as the sulfurization temperature reaches 500 °C or higher. Sulfurization at the temperatures higher than 500 °C leads to In coming from the ITO back contact diffusion into CZTS to a considerable extent, the formation of tin sulfides, and the degradation of ITO conductivity. These sulfurized films exhibit a double-layered structure, where the upper layers are constructed with large grained CZTIS/CZTS and the bottom layers consist of small grains with tin sulfides segregating. The grain size of the bottom/upper layer increases with sulfurization temperature, which ultimately results in amalgamation of bottom and upper absorber layers as well as the disappearance of ITO back contact. The new kesterite CZTIS alloy exhibits the identical band gap, the expanded lattice, and similar phonon spectra by analogy with the pure CZTS. On the other hand, the bifacial solar cells obtained by 520 °C sulfurization exhibit the best device performance. Sulfurization at the temperatures higher than 520 °C gave rise to the thorough degradation of ITO back contact, and therefore, no well-defined device results were obtained. The lower crystalline quality of the absorbers sulfurized at 500 °C led to the inferior device performance as opposed to the counterparts sulfurized at 520 °C. The device performance is still limited by the issues of high series resistance, low fill factor, and low open circuit voltage correlating with the non-ohmic back contact (secondary diode), the degraded conductivity of ITO back contact, the short minority lifetime, and the high interfacial recombination rates. A series of characterizations, analyses, and discussions regarding these device issues in conjunction with material characters and interfacial reaction processes are addressed, which are complementary to our previous work.[34]

DOI: 10.1021/acsami.5b01641
ACS Appl. Mater. Interfaces 2015, 7, 10414−10428

■ ASSOCIATED CONTENT

Supporting Information

XPS data of the CZTIS film on ITO substrate. XRD data of the CZTS films on Mo substrate and sulfurized ITO substrates. This material is available free of charge via the Internet at http://pubs.acs.org/.

■ AUTHOR INFORMATION

Corresponding Authors

*E-mail: Jie.Ge@utoledo.edu.
*E-mail: jhchu@mail.sitp.ac.cn.

Notes

The authors declare no competing financial interest.

■ ACKNOWLEDGMENTS

The financial support by the Knowledge Innovation Program of the Chinese Academy of Sciences (Y2K4401DG0), the National Science Foundation of USA (che-1230246), and the National Natural Science Foundation of China (61474045) are acknowledged.

■ DEDICATION

This manuscript is dedicated to Prof. Dr. Jun-Hao Chu on the Occasion of his 70th birthday in March 2015.

■ REFERENCES

(1) Kimball, G. M.; Lewis, N. S.; Atwater, H. A. In Mg Doping and Alloying in Zn3P2 Heterojunction Solar Cells. *Photovoltaic Specialists Conference (PVSC)*, 2010 35th IEEE, Honolulu, HI, 20−25 June 2010; pp 001039−001043.

(2) Vazquez−Mena, O.; Bosco, J. P.; Ergen, O.; Rasool, H. I.; Fathalizadeh, A.; Tosun, M.; Crommie, M.; Javey, A.; Atwater, H. A.; Zettl, A. Performance Enhancement of a Graphene−Zinc Phosphide Solar Cell Using the Electric Field−Effect. *Nano Lett.* **2014**, *14*, 4280−4285.

(3) Fukumoto, T.; Moehl, T.; Niwa, Y.; Nazeeruddin, M. K.; Grätzel, M.; Etgar, L. Effect of Interfacial Engineering in Solid−State Nanostructured Sb2S3 Heterojunction Solar Cells. *Adv. Energy Mater.* **2013**, *3*, 29−33.

(4) Zhou, Y.; Leng, M.; Xia, Z.; Zhong, J.; Song, H.; Liu, X.; Yang, B.; Zhang, J.; Chen, J.; Zhou, K.; Han, J.; Cheng, Y.; Tang, J. Solution−Processed Antimony Selenide Heterojunction Solar Cells. *Adv. Energy Mater.* **2014**, *4*, 1301846.

(5) Escorcia−García, J.; Becerra, D.; Nair, M. T. S.; Nair, P. K. Heterojunction CdS/Sb2S3 Solar Cells Using Antimony Sulfide Thin Films Prepared by Thermal Evaporation. *Thin Solid Films* **2014**, *569*, 28−34.

(6) Sinsermsuksakul, P.; Sun, L.; Lee, S. W.; Park, H. H.; Kim, S. B.; Yang, C.; Gordon, R. G. Overcoming Efficiency Limitations of SnS−Based Solar Cells. *Adv. Energy Mater.* **2014**, *4*, 1400496.

(7) Steinmann, V.; Jaramillo, R.; Hartman, K.; Chakraborty, R.; Brandt, R. E.; Poindexter, J. R.; Lee, Y. S.; Sun, L.; Polizzotti, A.; Park, H. H.; Gordon, R. G.; Buonassisi, T. 3.88% Efficient Tin Sulfide Solar Cells using Congruent Thermal Evaporation. *Adv. Mater.* **2014**, *26*, 7488−7492.

(8) Wangperawong, A.; Hsu, P.−C.; Yee, Y.; Herron, S. M.; Clemens, B. M.; Cui, Y.; Bent, S. F. Bifacial Solar Cell with SnS Absorber by Vapor Transport Deposition. *Appl. Phys. Lett.* **2014**, *105*, 173904.

(9) Yeon, D. H.; Lee, S. M.; Jo, Y. H.; Moon, J.; Cho, Y. S. Origin of the Enhanced Photovoltaic Characteristics of PbS Thin Film Solar Cells Processed at Near Room Temperature. *J. Mater. Chem. A* **2014**, *2*, 20112−20117.

(10) Richardson, B. J.; Zhu, L.; Yu, Q. Inverted Hybrid Solar Cells Based on Pyrite FeS2 Nanocrystals in P3HT:PCBM with Enhanced Photocurrent and Air−stability. *Sol. Energy Mater. Sol. Cells* **2013**, *116*, 252−261.

(11) Riha, S. C.; Jin, S.; Baryshev, S. V.; Thimsen, E.; Wiederrecht, G. P.; Martinson, A. B. F. Stabilizing Cu2S for Photovoltaics One Atomic Layer at a Time. *ACS Appl. Mater. Interfaces* **2013**, *5*, 10302−10309.

(12) Lee, Y. S.; Heo, J.; Siah, S. C.; Mailoa, J. P.; Brandt, R. E.; Kim, S. B.; Gordon, R. G.; Buonassisi, T. Ultrathin Amorphous Zinc−tin−oxide Buffer Layer for Enhancing Heterojunction Interface Quality in Metal−oxide Solar Cells. *Energy Environ. Sci.* **2013**, *6*, 2112−2118.

(13) Hoye, R. L. Z.; Heffernan, S.; Ievskaya, Y.; Sadhanala, A.; Flewitt, A.; Friend, R. H.; MacManus−Driscoll, J. L.; Musselman, K. P. Engineering Schottky Contacts in Open−Air Fabricated Heterojunction Solar Cells to Enable High Performance and Ohmic Charge Transport. *ACS Appl. Mater. Interfaces* **2014**, *6*, 22192−22198.

(14) Septina, W.; Ikeda, S.; Iga, Y.; Harada, T.; Matsumura, M. Thin Film Solar Cell Based on CuSbS2 Absorber Fabricated from an Electrochemically Deposited Metal Stack. *Thin Solid Films* **2014**, *550*, 700−704.

(15) Mitsutaro, U.; Yasuhiko, T.; Tomoyoshi, M.; Takenobu, S.; Hiroki, A.; Ryosuke, M. Cu2Sn1−xGexS3 (x = 0.17) Thin−film Solar Cells with High Conversion Efficiency of 6.0%. *App. Phys. Express* **2013**, *6*, 045501.

(16) Cho, J. W.; Ismail, A.; Park, S. J.; Kim, W.; Yoon, S.; Min, B. K. Synthesis of Cu2ZnSnS4 Thin Films by a Precursor Solution Paste for Thin Film Solar Cell Applications. *ACS Appl. Mater. Interfaces* **2013**, *5*, 4162−4165.

(17) Cui, J.; Meng, F.; Zhang, H.; Cao, K.; Yuan, H.; Cheng, Y.; Huang, F.; Wang, M. CH3NH3PbI3−Based Planar Solar Cells with Magnetron−Sputtered Nickel Oxide. *ACS Appl. Mater. Interfaces* **2014**, *6*, 22862−22870.

(18) Shi, J.; Luo, Y.; Wei, H.; Luo, J.; Dong, J.; Lv, S.; Xiao, J.; Xu, Y.; Zhu, L.; Xu, X.; Wu, H.; Li, D.; Meng, Q. Modified Two−Step Deposition Method for High−Efficiency TiO2/CH3NH3PbI3 Heterojunction Solar Cells. *ACS Appl. Mater. Interfaces* **2014**, *6*, 9711−9718.

(19) Liu, C.; Wang, K.; Du, P.; Meng, T.; Yu, X.; Cheng, S. Z. D.; Gong, X. High Performance Planar Heterojunction Perovskite Solar Cells with Fullerene Derivatives as the Electron Transport Layer. *ACS Appl. Mater. Interfaces* **2015**, *7*, 1153−1159.

(20) Sugimoto, H.; Hiroi, H.; Sakai, N.; Muraoka, S.; Katou, T. In Over 8% efficiency Cu2ZnSnS4 Submodules with Ultra-thin Absorber. *Photovoltaic Specialists Conference (PVSC)*, 2012 38th IEEE, Austin, TX, 3−8 June 2012; pp 002997−003000.

(21) Hiroi, H.; Sakai, N.; Kato, T.; Sugimoto, H. In High Voltage Cu2ZnSnS4 Submodules by Hybrid Buffer Layer. *Photovoltaic Specialists Conference (PVSC)*, 2013 IEEE 39th, Tampa, FL, 16−21 June 2013; pp 0863−0866.

(22) Sugimoto, H.; Liao, C.; Hiroi, H.; Sakai, N.; Kato, T. In Lifetime Improvement for High Efficiency Cu2ZnSnS4 Submodules. *Photovoltaic Specialists Conference (PVSC)*, 2013 IEEE 39th, Tampa, FL, 16−21 June 2013; pp 3208−3211.

(23) Shin, B.; Gunawan, O.; Zhu, Y.; Bojarczuk, N. A.; Chey, S. J.; Guha, S. Thin Film Solar Cell with 8.4% Power Conversion Efficiency using an Earth−abundant Cu2ZnSnS4 Absorber. *Prog. Photovoltaics* **2013**, *21*, 72−76.

(24) Ahmed, S.; Reuter, K. B.; Gunawan, O.; Guo, L.; Romankiw, L. T.; Deligianni, H. A High Efficiency Electrodeposited Cu2ZnSnS4 Solar Cell. *Adv. Energy Mater.* **2012**, *2*, 253−259.

(25) Jiang, F.; Ikeda, S.; Harada, T.; Matsumura, M. Pure Sulfide Cu2ZnSnS4 Thin Film Solar Cells Fabricated by Preheating an Electrodeposited Metallic Stack. *Adv. Energy Mater.* **2014**, *4*, 1301381.

(26) Scragg, J. J.; Kubart, T.; Wätjen, J. T.; Ericson, T.; Linnarsson, M. K.; Platzer−Björkman, C. Effects of Back Contact Instability on Cu2ZnSnS4 Devices and Processes. *Chem. Mater.* **2013**, *25*, 3162−3171.

(27) Tajima, S.; Itoh, T.; Hazama, H.; Ohishi, K.; Asahi, R. In Improvement of the Open−circuit Voltage of Cu2ZnSnS4 Cells using a Two−layered Process. *Photovoltaic Specialist Conference (PVSC)*, 2014 IEEE 40th, Denver, CO, 8−13 June 2014; pp 0431−0434.

DOI: 10.1021/acsami.5b01641
ACS Appl. Mater. Interfaces 2015, 7, 10414−10428

(28) Romanyuk, Y. E.; Hagendorfer, H.; Stücheli, P.; Fuchs, P.; Uhl, A. R.; Sutter−Fella, C. M.; Werner, M.; Haass, S.; Stückelberger, J.; Broussillou, C.; Grand, P.−P.; Bermudez, V.; Tiwari, A. N. All Solution−Processed Chalcogenide Solar Cells − from Single Functional Layers Towards a 13.8% Efficient CIGS Device. *Adv. Funct. Mater.* **2015**, *25*, 12−27.
(29) Colombara, D.; Crossay, A.; Vauche, L.; Jaime, S.; Arasimowicz, M.; Grand, P. P.; Dale, P. J. Electrodeposition of Kesterite Thin Films for Photovoltaic Applications: Quo Vadis? *Phys. Status Solidi A* **2015**, *212*, 88−102.
(30) Salomé, P. M. P.; Malaquias, J.; Fernandes, P. A.; Ferreira, M. S.; Leitão, J. P.; da Cunha, A. F.; González, J. C.; Matinaga, F. N.; Ribeiro, G. M.; Viana, E. R. The Influence of Hydrogen in the Incorporation of Zn during the Growth of Cu2ZnSnS4 Thin Films. *Sol. Energy Mater. Sol. Cells* **2011**, *95*, 3482−3489.
(31) Ennaoui, A.; Lux−Steiner, M.; Weber, A.; Abou−Ras, D.; Kötschau, I.; Schock, H. W.; Schurr, R.; Hölzing, A.; Jost, S.; Hock, R.; Voß, T.; Schulze, J.; Kirbs, A. Cu2ZnSnS4 Thin Film Solar Cells from Electroplated Precursors: Novel Low−cost Perspective. *Thin Solid Films* **2009**, *517*, 2511−2514.
(32) Ge, J.; Jiang, J.; Yang, P.; Peng, C.; Huang, Z.; Zuo, S.; Yang, L.; Chu, J. A 5.5% Efficient Co−electrodeposited ZnO/CdS/Cu2ZnSnS4/Mo Thin Film Solar Cell. *Sol. Energy Mater. Sol. Cells* **2014**, *125*, 20−26.
(33) Simchi, H.; Larsen, J.; Kihwan, K.; Shafarman, W. Improved Performance of Ultrathin Cu(InGa)Se2 Solar Cells With a Backwall Superstrate Configuration. *IEEE J. Photovolt.* **2014**, *4*, 1630−1635.
(34) Ge, J.; Chu, J.; Jiang, J.; Yan, Y.; Yang, P. Characteristics of In−Substituted CZTS Thin Film and Bifacial Solar Cell. *ACS Appl. Mater. Interfaces* **2014**, *6*, 21118−21130.
(35) Hartnauer, S.; Wägele, L. A.; Jarzembowski, E.; Scheer, R. In-situ XRD Study of Alloyed Cu2ZnSnSe4−CuInSe2 Thin Films for Solar Cells. *Thin Solid Films* **2015**, *582*, 272−275.
(36) McCarthy, R. F.; Weimer, M. S.; Emery, J. D.; Hock, A. S.; Martinson, A. B. F. Oxygen−Free Atomic Layer Deposition of Indium Sulfide. *ACS Appl. Mater. Interfaces* **2014**, *6*, 12137−12145.
(37) Ge, J.; Chu, J.; Jiang, J.; Yan, Y.; Yang, P. The Interfacial Reaction at ITO Back Contact in Kesterite Bifacial Solar Cells. *submitted* 2015.
(38) Burton, L. A.; Colombara, D.; Abellon, R. D.; Grozema, F. C.; Peter, L. M.; Savenije, T. J.; Dennler, G.; Walsh, A. Synthesis, Characterization, and Electronic Structure of Single−Crystal SnS, Sn2S3, and SnS2. *Chem. Mater.* **2013**, *25*, 4908−4916.
(39) Chen, S.-Y.; Gong, X.-G.; Walsh, A.; Wei, S.-H. Recent Progress in the Theoretical Study of Cu2ZnSnS4 and Related Chalcogenide Semiconductors. *Wuli* **2011**, *40*, 248−258.
(40) Mead, D. G.; Chandrasekhar, H. R. Far Infrared Optical Properties of SnIISnIVS3. *Infrared Phys.* **1980**, *20*, 245−247.
(41) Chandrasekhar, H. R.; Humphreys, R. G.; Zwick, U.; Cardona, M. Infrared and Raman Spectra of the IV−VI Compounds SnS and SnSe. *Phys. Rev. B* **1977**, *15*, 2177−2183.
(42) Lucovsky, G.; Mikkelsen, J. C.; Liang, W. Y.; White, R. M.; Martin, R. M. Optical Phonon Anisotropies in the Layer Crystals SnS2 and SnSe2. *Phys. Rev. B* **1976**, *14*, 1663−1669.
(43) Fontane, X.; Izquierdo-Roca, V.; Fairbrother, A.; Espindola-Rodriguez, M.; Lopez-Marino, S.; Placidi, M.; Jawhari, T.; Saucedo, E.; Perez-Rodriguez, A. In Selective Detection of Secondary Phases in Cu2ZnSn(S, Se) 4 Based Absorbers by Pre-resonant Raman Spectroscopy. *Photovoltaic Specialists Conference (PVSC)*, 2013 IEEE 39th, Tampa, FL, 16−21 June 2013; pp 2581−2584.
(44) Platzer-Björkman, C.; Scragg, J.; Flammersberger, H.; Kubart, T.; Edoff, M. Influence of Precursor Sulfur Content on Film Formation and Compositional Changes in Cu2ZnSnS4 Films and Solar Cells. *Sol. Energy Mater. Sol. Cells* **2012**, *98*, 110−117.
(45) Paris, M.; Choubrac, L.; Lafond, A.; Guillot-Deudon, C.; Jobic, S. Solid-State NMR and Raman Spectroscopy To Address the Local Structure of Defects and the Tricky Issue of the Cu/Zn Disorder in Cu-Poor, Zn-Rich CZTS Materials. *Inorg. Chem.* **2014**, *53*, 8646−8653.
(46) Scragg, J. J. S.; Choubrac, L.; Lafond, A.; Ericson, T.; Platzer−Björkman, C. A Low-Temperature Order−disorder Transition in Cu2ZnSnS4 Thin Films. *Appl. Phys. Lett.* **2014**, *104*, 041911.
(47) Dimitrievska, M.; Fairbrother, A.; Pérez−Rodríguez, A.; Saucedo, E.; Izquierdo−Roca, V. Raman Scattering Crystalline Assessment of Polycrystalline Cu2ZnSnS4 Thin Films for Sustainable Photovoltaic Technologies: Phonon Confinement Model. *Acta Mater.* **2014**, *70*, 272−280.
(48) Álvarez−García, J.; Izquierdo−Roca, V.; Pérez−Rodríguez, A. Raman Spectroscopy on Thin Films for Solar Cells. In *Advanced Characterization Techniques for Thin Film Solar Cells*; Wiley−VCH Verlag GmbH & Co. KGaA: Weinheim, Germany, 2011; pp 365−386.
(49) Gunawan, O.; Gokmen, T.; Mitzi, D. B. Suns−V_{OC} Characteristics of High Performance Kesterite Solar Cells. *J. Appl. Phys.* **2014**, *116*, 084504.
(50) Kim, J.; Hiroi, H.; Todorov, T. K.; Gunawan, O.; Kuwahara, M.; Gokmen, T.; Nair, D.; Hopstaken, M.; Shin, B.; Lee, Y. S.; Wang, W.; Sugimoto, H.; Mitzi, D. B. High Efficiency Cu2ZnSn(S,Se)4 Solar Cells by Applying a Double In2S3/CdS Emitter. *Adv. Mater.* **2014**, *26*, 7427−7431.
(51) Moore, J.; Hages, C. J.; Carter, N.; Agrawal, R.; Lundstrom, M. In The Physics of V_{bi}−related IV Crossover in Thin Film Solar Cells: Applications to Ink Deposited CZTSSe. *Photovoltaic Specialists Conference (PVSC)*, 2013 IEEE 39th, Tampa, FL, 16−21 June 2013; pp 3255−3259.
(52) Moore, J. E.; Dongaonkar, S.; Chavali, R. V. K.; Alam, M. A.; Lundstrom, M. S. Correlation of Built−In Potential and IV Crossover in Thin−Film Solar Cells. *IEEE J. Photovolt.* **2014**, *4*, 1138−1148.
(53) Gunawan, O.; Gokmen, T.; Shin, B. S.; Guha, S. In Device Characteristics of High Performance Cu2ZnSnS4 solar cell. *Photovoltaic Specialists Conference (PVSC)*, 2012 38th IEEE, Austin, TX, 3−8 June 2012; pp 003001−003003.
(54) Gokmen, T.; Gunawan, O.; Todorov, T. K.; Mitzi, D. B. Band Tailing and Efficiency Limitation in Kesterite Solar Cells. *Appl. Phys. Lett.* **2013**, *103*, 103506.
(55) Loef, R.; Schoonman, J.; Goossens, A. Elucidation of Homojunction Formation in CuInS2 with Impedance Spectroscopy. *J. Appl. Phys.* **2007**, *102*, 024512.
(56) Gunawan, O.; Gokmen, T.; Warren, C. W.; Cohen, J. D.; Todorov, T. K.; Barkhouse, D. A. R.; Bag, S.; Tang, J.; Shin, B.; Mitzi, D. B. Electronic Properties of the Cu2ZnSn(Se,S)4 Absorber Layer in Solar Cells as Revealed by Admittance Spectroscopy and Related Methods. *Appl. Phys. Lett.* **2012**, *100*, 253905.
(57) Koishiyev, G. T.; Sites, J. R.; Kulkarni, S. S.; Dhere, N. G. In Determination of Back Contact Barrier Height in Cu(In,Ga)(Se,S)2 and CdTe Solar Cells. *Photovoltaic Specialists Conference (PVSC)*, 33rd IEEE, San Diego, CA, 11−16 May 2008; pp 1−3.
(58) Burgelman, M.; Nollet, P.; Degrave, S. Electronic Behaviour of Thin−film CdTe Solar Cells. *Appl. Phys. A: Mater. Sci. Process.* **1999**, *69*, 149−153.
(59) Verschraegen, J.; Burgelman, M.; Penndorf, J. Interpretation of Capacitance Measurements in $CuInS_2$-on-Cu-tape Solar Cells. *Thin Solid Films* **2004**, *451−452*, 179−183.
(60) Schlenker, E.; Mertens, V.; Parisi, J.; Reineke−Koch, R.; Köntges, M. Schottky Contact Analysis of Photovoltaic Chalcopyrite Thin Film Absorbers. *Phys. Lett. A* **2007**, *362*, 229−233.
(61) Sánchez-Juárez, A.; Tiburcio-Silver, A.; Ortiz, A. Fabrication of SnS_2/SnS Heterojunction Thin Film Diodes by Plasma-enhanced Chemical Vapor Deposition. *Thin Solid Films* **2005**, *480−481*, 452−456.
(62) Chen, S.; Walsh, A.; Yang, J.-H.; Gong, X. G.; Sun, L.; Yang, P.-X.; Chu, J.-H.; Wei, S.-H. Compositional Dependence of Structural and Electronic Properties of Cu2ZnSn(S,Se)4 Alloys for Thin Film Solar Cells. *Phys. Rev. B* **2011**, *83*, 125201.
(63) Xie, H.; Sánchez, Y.; López-Marino, S.; Espíndola-Rodríguez, M.; Neuschitzer, M.; Sylla, D.; Fairbrother, A.; Izquierdo-Roca, V.; Pérez-Rodríguez, A.; Saucedo, E. Impact of Sn(S,Se) Secondary Phases in Cu2ZnSn(S,Se)4 Solar Cells: A Chemical Route for Their Selective

DOI: 10.1021/acsami.5b01641
ACS Appl. Mater. Interfaces 2015, 7, 10414−10428

Removal and Absorber Surface Passivation. *ACS Appl. Mater. Interfaces* **2014**, *6*, 12744−12751.
(64) Ham, G.; Shin, S.; Park, J.; Choi, H.; Kim, J.; Lee, Y.-A.; Seo, H.; Jeon, H. Tuning the Electronic Structure of Tin Sulfides Grown by Atomic Layer Deposition. *ACS Appl. Mater. Interfaces* **2013**, *5*, 8889−8896.

DOI: 10.1021/acsami.5b01641
ACS Appl. Mater. Interfaces 2015, 7, 10414−10428